

ARTICLE OPEN



Time-dependent density-functional theory molecular-dynamics study on amorphization of Sc-Sb-Te alloy under optical excitation

Xue-Peng Wang¹, Xian-Bin Li¹, Nian-Ke Chen¹, Junhyeok Bang², Ryky Nelson³, Christina Ertural³, Richard Dronskowski^{3,4}, Hong-Bo Sun^{1,5} and Shengbai Zhang⁶

Recently, all-optical memory and optical-computation properties of phase-change materials are receiving intensive attention. Because writing/erasing information in these devices is usually achieved by laser pulses, the interaction between the laser and the phase-change materials becomes a key issue for such new applications. In this work, by a time-dependent density-functional theory molecular-dynamics study, the physics underlying the optical excitation induced amorphization of Sc-Sb-Te is revealed, which goes back to superatom-like Sc-centered structural motifs. These motifs are found to be still robust under the excitation. A selected occupation of the Sc $d-t_{2g}$ orbitals (as a result of optical excitation) leads to a significant change of Sc-centered bond angles. In addition, the especially weak Sb-Te bonds next to the Sc motifs are further diminished by excitations. Therefore, the Sc-centered motifs can promote breaking, switching, and reforming of the surrounding Sb-Te network and, therefore, facilitate the amorphization of Sc-Sb-Te. The study shows the unique role of Sc-centered motifs in optically induced phase transition, and displays potential applications of Sc-Sb-Te alloys in optical memory/computation.

npj Computational Materials (2020)6:31 | <https://doi.org/10.1038/s41524-020-0303-z>

INTRODUCTION

Phase-change memory (PCM) materials work by switching between their amorphous and crystalline phases under an appropriate electrical or laser pulse^{1–5}. At the same time, the great contrasts in resistance and refractive index/reflectivity between the two phases ensure the applications of PCM materials in both non-volatile electrical and optical memory^{6–10}. The commercial applications of PCM materials in optical disks started in the 1980s already¹. In the past decade, however, PCM materials have been employed to develop electrical memories¹¹. In the most recent years, optical applications based on PCM materials are also receiving intensive attention. By combining a PCM material ($\text{Ge}_2\text{Sb}_2\text{Te}_5$, GST) and optical fibers, a non-volatile all-optical multi-level memory has been achieved by Ríos et al.¹². Both writing/erasing and reading information in the GST memory are performed by laser pulses (typically, 100-ns duration for the writing/erasing) in fiber via evanescent coupling to the GST. In 2019, Feldmann et al. have demonstrated an all-optical spiking neurosynaptic networks being able of photonic neuromorphic computation using laser pulses¹³. Also, other optical/photonic applications with PCM materials, such as active plasmonics and metamaterials, have been reported recently^{14–16}.

In the optical PCM devices mentioned above, laser pulses are used to induce phase transition in PCM materials. Therefore, the interaction between the laser and the material is the key issue for these new applications. It is generally believed that a laser pulse induces the phase change through thermal effects, such as melt-quenched amorphization^{4,17}, caused by carrier-phonon coupling. At the same time, the non-thermal effect of a laser, such as coherent

optical phonons excitation^{18,19}, and plasma annealing^{20–22}, could also affect the bonding network^{23,24}, and offer another driving force²⁵ for fast phase change in optical data storage.

Sc-Sb-Te is a rising-star PCM material to hold the record-breaking sub-ns crystallization speed. This kind of material is firstly proposed by F. Rao et al. in 2017²⁶. It has been demonstrated that the Sc-centered motifs present a high stability in both liquid and amorphous phases of Sc-Sb-Te²⁷. Therefore, these motifs could act as precursors of nuclei and thus achieve an ultrafast crystallization speed²⁶. Such a fast crystallization speed, which is also required in PCM material-based optical memory and computation devices²⁸, implies that Sc-Sb-Te can be a potential material for such applications. In this work, we study the amorphization mechanism of Sc-Sb-Te under optical excitation by time-dependent density-functional theory molecular dynamics (TDDFT-MD). Our results reveal the unique role of Sc-centered motifs, which are not only robust under intense laser excitation but whose existence promotes the amorphization process. Critically important, however, is the so-far unrecognized role of the excitation, which increases the occupation of Sc $d-t_{2g}$ orbitals. Therefore, a rapid distortion of the excited motifs could facilitate an amorphization within 1 ps at a 9% excitation. In other words, Sc-Sb-Te and also other transition metal (TM) embedded PCM materials not only improve the SET (crystallization) process but also the RESET (amorphization) process, whereby potentially optimizing their optical memory/computation applications.

The paper is organized as follows: in the “Results and discussion” section, first, we show the structural evolution upon different amount of excitation (Fig. 1). Then, we analyze the effect

¹State Key Laboratory of Integrated Optoelectronics, College of Electronic Science and Engineering, Jilin University, 130012 Changchun, China. ²Department of Physics, Chungbuk National University, 28644 Chungbuk, Republic of Korea. ³Institute of Inorganic Chemistry, RWTH Aachen University, 52056 Aachen, Germany. ⁴Hoffmann Institute of Advanced Materials, Shenzhen Polytechnic, 518055 Shenzhen, China. ⁵State Key Lab of Precision Measurement Technology and Instruments Department of Precision Instrument, Tsinghua University, 100084 Beijing, China. ⁶Department of Physics, Applied Physics, and Astronomy, Rensselaer Polytechnic Institute, Troy, NY 12180, USA. ✉email: lixianbin@jlu.edu.cn; hbsun@tsinghua.edu.cn; zhangs9@rpi.edu

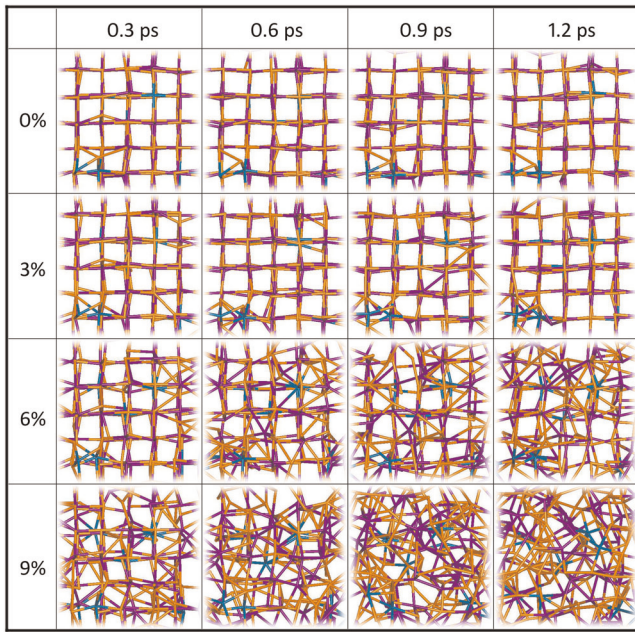


Fig. 1 Structural evolution of Sc-Sb-Te upon optical excitation. Structures (in a bond stick model) of rocksalt Sc-Sb-Te under optical excitation of valence electrons from 0 to 9% (rows) at 0.3, 0.6, 0.9, and 1.2 ps (columns), respectively. Color coding: Cyan for Sc, purple for Sb, and orange for Te.

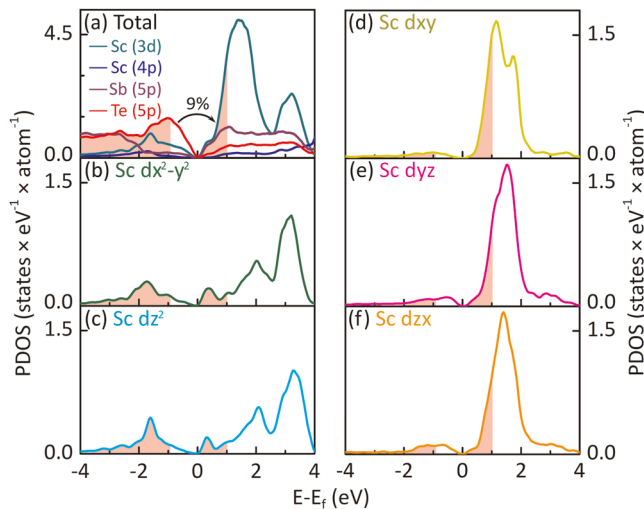


Fig. 2 Density of states of rocksalt Sc-Sb-Te. **a** Partial density of states (PDOS) per atom of Sc, Sb, and Te near the band edges. For simplicity, we have ignored the small amounts of *s* states. **b–f** The *d* states of Sc decomposed into **b** $d_{x^2-y^2}$ and **c** d_{z^2} orbitals (of crystal e_g orbitals) and **d** d_{xy} , **e** d_{yz} , and **f** d_{zx} orbitals (of crystal t_{2g} orbitals). Pink shaded areas are the occupations for a 9% optical excitation.

of optical excitation on electronic structure of Sc-Sb-Te (Fig. 2) and Sc bonding configuration (Fig. 3). Next, the robust feature of Sc-centered motifs upon excitation is illustrated (Fig. 4). Based on these results, we propose the unique role of Sc-centered motifs in amorphization of Sc-Sb-Te upon excitation (Fig. 5). The summary and discussions about possible applications of our results are given at the end of this section. Finally, in the “Methods” section, details of our calculations including modeling process, simulations parameters, and analysis methods of electronic structure are introduced.

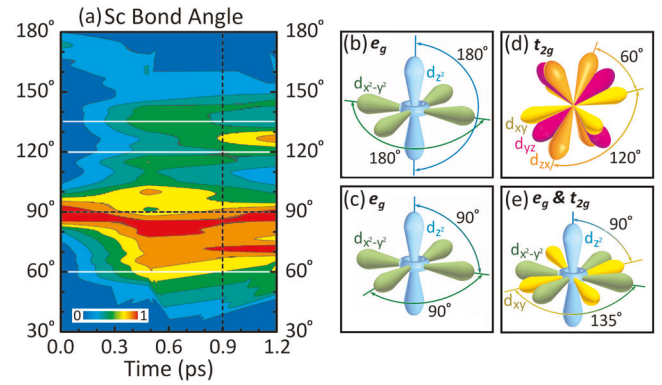


Fig. 3 Bonding configuration of Sc-centered motif upon excitation. **a** Time evolution of (normalized) bond angle distribution (BAD) of Sc under a 9% excitation. Color bar indicates the BAD intensity: the blue and red stand for weak and strong intensity, respectively. **b, c** Charge lobes of the e_g orbitals. Notice the 180° angles in **(b)** and 90° angles in **(c)** between the lobes. They are characteristic of the bond angles in rocksalt Sc-Sb-Te. **d** Charge lobes of the t_{2g} orbitals. Notice the 60° and 120° angles between the lobes. **e** Angles formed between the charge lobes of e_g and t_{2g} . For simplicity, only the d_{xy} orbital is shown. The characteristic angles here are the 90° angles between d_{xy} and d_{z^2} and the 135° angles between d_{xy} and $d_{x^2-y^2}$. In **a**, the crystalline 90° angles are denoted by a black dashed line, while the characteristic 60°, 120°, and 135° angles are denoted by white solid lines.

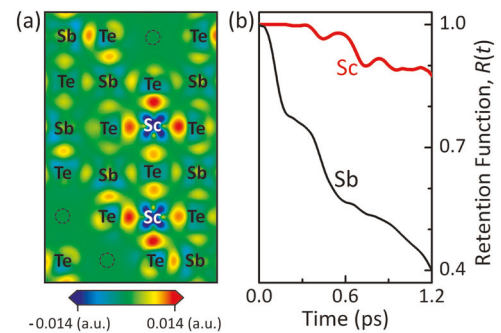


Fig. 4 Stability of Sc-centered motif in the ground state and excited state. **a** Difference between the self-consistent charge and a superposition of atomic charges (charge density difference, CDD) in a (001) plane for rocksalt Sc-Sb-Te. In the plot, dashed circles denote cation vacancies. Color bar indicates the CDD intensity: red for the positive and blue for the negative intensity. **b** Time evolution of the (average) original neighbor-retention function $R(t)$ during amorphization at a 9% excitation.

RESULTS AND DISCUSSION

Structural evolution upon excitation

Figure 1 shows the amorphization of Sc-Sb-Te as a function of time at various amounts of excitations of valence electrons. More details about the amounts of excitations are given in the “Methods” section. In the simulation, we preheat the rocksalt Sc-Sb-Te to 300 K for 3 ps ahead of the excitation, followed by TDDFT-MD with excitations to 1.2 ps. The excitation effects are given in Fig. 1: for 0% excitation (ground state), no sign of disorder occurs at 1.2 ps; for 3% excitation, the system maintains as a whole the rocksalt structure at 1.2 ps, except for some distortions around the Sc atoms; for 6% excitation, significant disorder can be observed at 1.2 ps (The significantly disordered structure here will transform back into a crystalline phase after a de-excitation structural optimization. So, amorphization does not complete at this moment. See Supplementary Fig. 1 for more details); for 9%

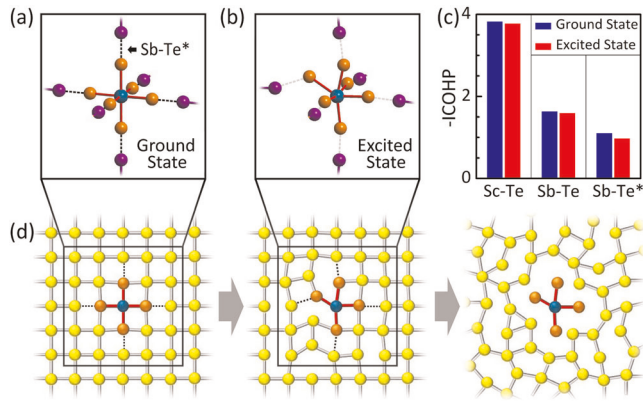


Fig. 5 Sc-centered motif facilitates amorphization of Sc-Sb-Te. Schematic drawings of the Sc-centered motifs **a** in the ground state octahedral coordination (the weak Sb-Te* bond next to Sc-Te bond in a line denoted by dashed lines) and **b** in the excited state. **c** Integration of crystal orbital Hamilton population (ICOHP) to reflect the strength of the Sc-Te bonds, Sb-Te* bonds, and the other Sb-Te bonds (not next to Sc-Te bonds) in the ground state (blue) and in the excited state (9% excitation, red), respectively. **d** Schematic drawings of the Sc-centered motif facilitating amorphization of Sc-Sb-Te. To clearly show the role of the motif in **d**, the Sc-centered motif is highlighted by the colorful balls as well as red sticks while the other atoms are all shown with yellow balls.

excitation, we estimate that the amorphization is achieved within 0.9 ps.

Excitation induced electronic selective occupation and bonding configuration change

To understand this ultrafast amorphization, Fig. 2a depicts the partial density of states (PDOS) per atom around band edges for Sc, Sb, and Te in the rocksalt phase. It shows that in the valence band the (anionic) Te p states dominate, while in the conduction band the (cationic) Sc d states are prominent instead. In other words, under an excitation, the Sc d states will be selectively occupied at the expense of the Te p states. Compared to the widely-studied Ge-Sb-Te systems²⁹, the Sc-Sb-Te system here is unique due to the replacement of Ge by Sc, which is the earliest transition metal. Therefore, the selective occupation of the Sc d states can be related to the ultrafast amorphization revealed in Fig. 1. For this reason, Fig. 2b–f depict the Sc d states in terms of e_g ($d_{x^2-y^2}$ and d_{z^2}) and t_{2g} (d_{xy} , d_{yz} and d_{zx}) orbitals. For a TM atom in a local octahedral environment, the e_g orbitals are higher in energy than the t_{2g} orbitals due to crystal-field splitting³⁰. As expected, Fig. 2b–f show that the major peaks of the $d_{x^2-y^2}$ and d_{z^2} orbitals lie above those of the d_{xy} , d_{yz} and d_{zx} orbitals in the conduction band.

For a more in-depth analysis, Fig. 3a traces the dynamics of the Sc-centered bond angle distribution (BAD) for the 9% excitation. Ideally, a rocksalt structure should have the 90° and 180° bond angles. However, rocksalt-like Sc-Sb-Te contains cation (Sc/Sb) vacancies, making the initial bond angles in Fig. 3a non-ideal, leaving the 90° angle the only primary angle. Upon excitation, the 90° angles split: one branch drifts down from 90° to roughly 80° and then further split into two sub-branches, one returns back to 90° while the other continues its downward drift to roughly 70°. The other branch at the start drifts up to roughly 130°. In accordance with the amorphization at 9% excitation in Fig. 1, after about 0.9 ps, these angles consolidate with increased intensities. To summarize, the Sc-centered bond angles change from the original 90° to approximately 70°, 90°, and 130° in the amorphous structure. We also calculate a bond angle distribution difference to

make the change of the bond angles more obvious under the excitation, see Supplementary Fig. 2 for more details.

As shown in Fig. 2, upon electronic excitation, electrons are mainly removed from Te p orbitals to Sc t_{2g} orbitals (i.e., d_{xy} , d_{yz} and d_{zx}). This hints to a possible correlation between the occupation of the Sc d orbitals and the observed Sc-centered bond angle changes in Fig. 3a. To examine, Fig. 3b and c displays the Sc-centered angles between $d_{x^2-y^2}$ and d_{z^2} , i.e., the two e_g orbitals (90° and 180°) while Fig. 3d shows the angles between any two t_{2g} orbitals (60° and 120°); in addition, Fig. 3e visualizes the angles between the e_g orbitals and one of the t_{2g} orbitals (90° and 135°). Note that the e_g orbitals are symmetry-adapted to the Sc local octahedral structure in the rocksalt structure so they hybridize to some degree with the Te p orbitals and get occupied in Fig. 2b, c, while the t_{2g} orbitals are energetically too far away such that they remain largely empty in Fig. 2d–f.

Should the amorphization be a result of the occupation changes, one would expect the Sc-centered bond angle to change from the original primary angle of 90° to 60°, 90°, 120°, and 135° of the amorphous structure. By comparison, we see that the 70° in Fig. 3a is a reminiscence of the 60° in Fig. 3d, the 90° in Fig. 3a is a reminiscence of the 90° in Fig. 3c, e, and the 130° in Fig. 3a could be a mixture of the 120° in Fig. 3d and 135° in Fig. 3e. Note that, due to the structural complexity of the amorphous structure, the comparison here can only be semi-quantitative. On the other hand, Supplementary Figs. 3 and 4 exemplify the effect without the excitation: for example, for an annealing of 3.6 ps even at 1100 K, the primary 90° bond angles stay largely unchanged. This difference confirms the role of optical excitation on ultrafast amorphization.

Strong superatom-like Sc-centered motifs still exist under excitations

In the Ge-Sb-Te systems such as GST, an intense excitation such as 9% could also induce a quick amorphization, in which Ge is found to play a key role²¹. This raises the question about the special role of Sc in Sc-Sb-Te during the fast amorphization processes. One answer lies in the different bond strengths. For Sc-Sb-Te, Fig. 4a shows the difference between the self-consistent charge and superposition of atomic charges (known as charge density difference, CDD) which serves as a measure of bond strength³¹. Figure 4a makes it clear that Sc always holds significantly more charge in its bonds with Te than Sb does. The notion that TM elements act as robust pinning sites in PCM materials was proposed in a previous study of Ti-Sb-Te³² and has been invoked to explain the rapid crystallization of Sc-Sb-Te^{26,27}. Evidently, it may also play a positive role for the amorphization observed here.

To quantify the aforementioned arguments, we define an (average) original neighbor-retention function $R(t)$, which measures how many original neighboring Te atoms of a cation have been retained during the amorphization,

$$R(t) = \frac{1}{n} \sum_{i=1}^n \frac{N_{it}}{N_{i0}} \quad (1)$$

where N_{i0} is the number of initial neighbors and N_{it} is the number remaining at time t . The average runs over n cationic atoms of concern, Sc or Sb in the supercell. Figure 4b shows $R(t)$ for Sc and Sb, respectively. Note that with a 9% excitation, $R(t)$ for Sc maintains at about 90% at the end of the simulation, while that for Sb at 40% is smaller by a factor of two. (Supplementary Fig. 5 shows that the semi-quantitative conclusion here does not depend on the choice of cutoffs for the bond lengths.) Such a large difference implies that during amorphization, extensive bond breaking has taken place around the Sb but not around the Sc atoms simply because of the stronger bonds that Sc can form with Te. Because of that bond rigidity, it is tempting to

consider Sc and its six Te neighbors to form a superatom-like Sc-centered motif.

Sc-centered motifs promote amorphization of Sc-Sb-Te

In addition, as described in Fig. 4a, the Sc-Te bonds hold more charge. This may indicate that the Sc-Te bonds gain charge from the neighboring Sb-Te bonds in a line³³, identified as Sb-Te* bonds in Fig. 5a. Such a charge transfer will then weaken the Sb-Te* bonds. In fact, an integration of the crystal orbital Hamilton population (ICOHP) to quantitatively measure the covalent bonding strength³⁴ given in Fig. 5c certainly demonstrates the weakness of the Sb-Te* bonds in the ground state compared with those other Sb-Te bonds not being next to the Sc-Te bonds. The crystal orbital Hamilton populations (COHP)³⁵ of these bonds for calculating the ICOHP data are given in Supplementary Fig. 6. Furthermore, the ICOHP for the (9%) excitation state shows these Sb-Te* bonds are further weakened by excitation compared with other Sb-Te bonds. Likewise, the ICOHP analysis also demonstrates that Sc has strong bonds with Te in both ground state and excited state. This matches the results from the CDD and $R(t)$ discussion in Fig. 4. Therefore, the amorphization process of Sc-Sb-Te can be schematically summarized (see Fig. 5d) as follows: upon excitation during which the Sc $d-t_{2g}$ orbitals are selectively occupied, a significant deviation of the bond angles from the original 90° of the Sc-centered motifs happens such as to instantly respond to the change in electronic structure. These distorted Sc-centered motifs, as shown in Fig. 5b, will promote breaking, switching of the surrounding Sb-Te network via the Sb-Te* bonds, and also reforming new Sb-Te bonds to facilitate the amorphization.

In conclusion, a TDDFT-MD study clarifies the microscopic process of Sc-Sb-Te amorphization under an optical excitation. The Sc-centered structural motifs become distorted due to an excitation-selected $d-t_{2g}$ orbital occupation. The distortion results in selectively breaking, switching, and reforming of the Sb-Te network close to the motif, while leaving the central Sc-Te bonds of the Sc-centered motifs largely intact. As such, the superatom-like motifs, already known for ultrafast recrystallization, also significantly promote amorphization. Note that cation vacancies can also facilitate the amorphization in PCM materials^{36,37} but in the present case the unique role of the Sc-centered motifs on the excited amorphization is clearly illustrated. This work indicates that the superior Sc-Sb-Te materials are not only suitable for SET operation²⁶ but also appropriate for RESET operation, which could improve their applications in the developing next-generation optical memory and optical computation.

METHODS

Modeling and parameters for TDDFT calculation

To model the Sc-Sb-Te system, we use a rocksalt supercell of composition $\text{Sc}_8\text{Sb}_{64}\text{Te}_{108}$, which is reasonably close to the experimentally determined composition of $\text{Sc}_{0.2}\text{Sb}_{1.8}\text{Te}_3$ pseudobinary alloy (between Sc_2Te_3 and Sb_2Te_3)²⁶. Our TDDFT-MD study employs the methodology developed by Meng and Kaxiras, as implemented in the SIESTA code³⁸, with norm-conserving Troullier-Martins pseudopotentials³⁹, Perdew-Burke-Ernzerhof (PBE) functional⁴⁰, and the NVE ensemble. The local basis set with double- ζ polarized orbitals is employed and the plane-wave energy cutoff is 100 Ry. The Ehrenfest approximation⁴¹ is used to couple the atomic and electronic motions. Even though the Ehrenfest dynamics have a drawback in describing the nuclear dynamics, it will not affect the qualitative results in the present study. Please see Part VI of Supplementary Information for more detailed discussions. In the TDDFT-MD simulation, we use a 0.024-fs time step. The calculation model of Sc-Sb-Te is maintained for 3 ps by ab initio MD at 300 K (without excitation) to obtain an equilibrium state as the TDDFT-MD input.

Initial excited state

For the initial excited state of electrons, we assume that the excited electronic population is ramped up to its stationary value instantaneously. And the electrons near the top of valance band are moved to the bottom part of conduction band as the initial state of photoexcitation (see the PDOS in Fig. 2a). However, based on the simplified method, we could also obtain some results which are consistent with experiments, as demonstrated in previous works^{20,25}. According to the pseudopotential used in present studies, Sc, Sb, and Te have 3, 5, and 6 valence electrons, respectively. Thus, the calculation model contains 992 valence electrons in total. The various amount of excitation (0, 3, 6, and 9% in Fig. 1) is realized by controlling the amount of total valence electrons moved to conduction band. Taking 9% excitation as an example, as illustrated in Fig. 2a, 90 electrons near the top of valance band ($E_f - 0.93$ eV to E_f) are moved to the bottom part of conduction band (E_f to $E_f + 1.01$ eV).

Analysis method for electronic and bonding structure

Static DFT calculations are performed within the projector-augmented wave (PAW) formalism⁴², as implemented in the VASP codes⁴³ with a 290-eV cutoff energy for the plane-wave basis set. The Local Orbital Basis Suite Towards Electronic-Structure Reconstruction (LOBSTER) code^{44,45} is used to analyze the PDOS and COHP. For the LOBSTER analysis, we use the contracted Slater-type orbitals (STO) basis functions of 3d 4s 4p, 5s 5p, and 5s 5p for Sc, Sb, and Te, respectively, when fitting the PAW wavefunctions calculated by VASP⁴⁶. The cutoff of bond length for structural analysis, i.e. bond angle distribution and $R(t)$, is 1.3× the sum of covalent radii between any two atoms. If the distance between two atoms is shorter than the cutoff, the two atoms are considered to bond with or be neighbors of each other.

DATA AVAILABILITY

The data that support the findings of this study are available from the corresponding author, Professor Xian-Bin Li (email: lixianbin@jlu.edu.cn), Professor Hong-Bo Sun (email: hbsun@tsinghua.edu.cn), and Professor Shengbai Zhang (email: zhangs9@rpi.edu) upon reasonable request.

Received: 14 October 2019; Accepted: 10 March 2020;

Published online: 08 April 2020

REFERENCES

- Wuttig, M. & Yamada, N. Phase-change materials for rewriteable data storage. *Nat. Mater.* **6**, 824–832 (2007).
- Li, X. B., Chen, N. K., Wang, X. P. & Sun, H. B. Phase-change superlattice materials toward low power consumption and high density data storage: microscopic picture, working principles, and optimization. *Adv. Funct. Mater.* **28**, 1803380 (2018).
- Xu, K. L., Miao, X. S. & Xu, M. The structure of phase-change chalcogenides and their high-pressure behavior. *Phys. Status Solidi Rrl.* **13**, 1800506 (2019).
- Roux, S. et al. Phase change materials and their application to random access memory technology. *Microelectron. Eng.* **85**, 2330–2333 (2008).
- Qu, Y. R. et al. Thermal camouflage based on the phase-changing material GST. *Light Sci. Appl.* **7**, 26 (2018).
- Fong, S. W., Neumann, C. N. & Philip Wong, H.-S. Phase-change memory - toward a storage-class memory. *IEEE Trans. Electron. Devices* **64**, 4374–4385 (2017).
- Sebastian, A. et al. Temporal correlation detection using computational phase-change memory. *Nat. Commun.* **8**, 1115 (2017).
- Tuma, T., Pantazi, A., Gallo, M. L., Sebastian, A. & Eleftheriou, E. Stochastic phase-change neurons. *Nat. Nanotechnol.* **11**, 693–699 (2016).
- Hegedüs, J. & Elliott, S. R. Microscopic origin of the fast crystallization ability of Ge-Sb-Te phase-change memory materials. *Nat. Mater.* **7**, 399–405 (2008).
- Du, K. K. et al. Control over emissivity of zero-static-power thermal emitters based on phase-changing material GST. *Light Sci. Appl.* **6**, e16194 (2017).
- Zhang, W., Mазzarelli, R., Wuttig, M. & Ma, E. Designing crystallization in phase-change materials for universal memory and neuro-inspired computing. *Nat. Rev. Mater.* **4**, 150–168 (2019).
- Rios, C. et al. Integrated all-photon non-volatile multi-level memory. *Nat. Photon.* **9**, 725–732 (2015).
- Feldmann, J., Youngblood, N., David Wright, C., Bhaskaran, H. & Pernice, W. H. P. All-optical spiking neurosynaptic networks with self-learning capabilities. *Nature* **596**, 208–214 (2019).

14. Wuttig, M., Bhaskaran, H. & Taubner, T. Phase-change materials for non-volatile photonic applications. *Nat. Photon.* **11**, 465–476 (2017).
15. Wang, Q. et al. Optically reconfigurable metasurfaces and photonic devices based on phase change materials. *Nat. Photon.* **10**, 60–65 (2015).
16. Yin, X. H. et al. Beam switching and bifocal zoom lensing using active plasmonic metasurfaces. *Light Sci. Appl.* **6**, e17016 (2017).
17. Siegel, J., Schropp, A., Solis, J., Afonso, C. N. & Wuttig, M. Rewritable phase-change optical recording in Ge₂Sb₂Te₅ films induced by picosecond laser pulses. *Appl. Phys. Lett.* **84**, 2250–2252 (2004).
18. Makino, K. et al. Anisotropic lattice response induced by a linearly-polarized femtosecond optical pulse excitation in interfacial phase change memory material. *Sci. Rep.* **6**, 19758 (2016).
19. Makino, K., Tominaga, J. & Hase, M. Ultrafast optical manipulation of atomic arrangements in chalcogenide alloy memory materials. *Opt. Express* **19**, 1260–1270 (2011).
20. Li, X. B., Liu, X. Q., Han, X. D. & Zhang, S. B. Role of electronic excitation in phase-change memory materials: a brief review. *Phys. Status Solidi B* **249**, 1861–1866 (2012).
21. Li, X. B. et al. Role of Electronic excitation in the amorphization of Ge-Sb-Te Alloys. *Phys. Rev. Lett.* **107**, 015501 (2011).
22. Bang, J., Sun, Y. Y., Liu, X. Q., Gao, F. & Zhang, S. B. Carrier-multiplication-induced structural change during ultrafast carrier relaxation and nonthermal phase transition in semiconductors. *Phys. Rev. Lett.* **117**, 126402 (2016).
23. Mitrofanov, K. V. et al. Sub-nanometre resolution of atomic motion during electronic excitation in phase-change materials. *Sci. Rep.* **6**, 20633 (2016).
24. Waldecker, L. et al. Time-domain separation of optical properties from structural transitions in resonantly bonded materials. *Nat. Mater.* **14**, 991–995 (2015).
25. Chen, N. K. et al. Directional forces by momentumless excitation and order-to-order transition in peierls-distorted solids: the case of GeTe. *Phys. Rev. Lett.* **120**, 185701 (2018).
26. Rao, F. et al. Reducing the stochasticity of crystal nucleation to enable sub-nanosecond memory writing. *Science* **358**, 1423–1427 (2017).
27. Qiao, C. et al. Local structure origin of ultrafast crystallization driven by high-fidelity octahedral clusters in amorphous Sc_{0.2}Sb₂Te₃. *Appl. Phys. Lett.* **114**, 071901 (2019).
28. Burr, G. W. A role for optics in AI hardware. *Nature* **569**, 199–200 (2019).
29. Yamada, N., Ohno, E., Nishiuchi, K., Akahira, N. & Takao, M. Rapid-phase transitions of GeTe-Sb₂Te₃ pseudobinary amorphous thin-films for an optical disk memory. *J. Appl. Phys.* **69**, 2849–2856 (1991).
30. Tokura, Y. & Nagaosa, N. Orbital physics in transition-metal oxides. *Science* **288**, 462–468 (2000).
31. Kolobov, A. V., Fons, P., Tominaga, J. & Ovshinsky, S. R. Vacancy-mediated three-center four-electron bonds in GeTe-Sb₂Te₃ phase-change memory alloys. *Phys. Rev. B* **87**, 165206 (2013).
32. Zhu, M. et al. One order of magnitude faster phase change at reduced power in Ti-Sb-Te. *Nat. Commun.* **5**, 4086 (2014).
33. Chen, N. K. et al. Strong electron-polarized atom chain in amorphous phase-change memory Ge-Sb-Te alloy. *Acta Mater.* **143**, 102–106 (2018).
34. Deringer, V. L., Stoffel, R. P., Wuttig, M. & Dronskowski, R. Vibrational properties and bonding nature of Sb₂Se₃ and their implications for chalcogenide materials. *Chem. Sci.* **6**, 5255 (2015).
35. Dronskowski, R. & Blöchl, P. E. Crystal orbital Hamilton populations (COHP). Energy-resolved visualization of chemical bonding in solids based on density-functional calculations. *J. Phys. Chem.* **97**, 8617–8624 (1993).
36. Fons, P. et al. Photoassisted amorphization of the phase-change memory alloy Ge₂Sb₂Te₅. *Phys. Rev. B* **82**, 041203(R) (2010).
37. Chen, N. K. et al. Giant lattice expansion by quantum stress and universal atomic forces in semiconductors under instant ultrafast laser excitation. *Phys. Chem. Chem. Phys.* **19**, 24735–24741 (2017).
38. Meng, S. & Kaxiras, E. Real-time, local basis-set implementation of time-dependent density functional theory for excited state dynamics simulations. *J. Chem. Phys.* **129**, 054110 (2008).
39. Troullier, N. & Martins, J. L. Efficient pseudopotentials for plane-wave calculations. *Phys. Rev. B* **43**, 1993 (1991).
40. Perdew, J. P., Burke, K. & Ernzerhof, M. Generalized gradient approximation made simple. *Phys. Rev. Lett.* **77**, 3865 (1997).
41. Alonso, J. L. et al. Efficient formalism for large-scale ab initio molecular dynamics based on time-dependent density functional theory. *Phys. Rev. Lett.* **101**, 096403 (2008).
42. Blöchl, P. E. Projector augmented-wave method. *Phys. Rev. B* **50**, 17953–17979 (1994).
43. Kresse, G. & Furthmüller, J. Efficient iterative schemes for ab initio total-energy calculations using a plane-wave basis set. *Phys. Rev. B* **54**, 11169 (1996).
44. Maintz, S., Deringer, V. L., Tchougréeff, A. L. & Dronskowski, R. Analytic projection from plane-wave and PAW wavefunctions and application to chemical-bonding analysis in solids. *J. Comput. Chem.* **34**, 2557–2567 (2013).
45. Maintz, S., Deringer, V. L., Tchougréeff, A. L. & Dronskowski, R. LOBSTER: A tool to extract chemical bonding from plane-wave based DFT. *J. Comput. Chem.* **37**, 1030–1035 (2016).
46. Deringer, V. L., Tchougréeff, A. L. & Dronskowski, R. Crystal orbital Hamilton population (COHP) analysis as projected from plane-wave basis sets. *J. Phys. Chem. A* **115**, 5461–5466 (2011).

ACKNOWLEDGEMENTS

Work in China was supported by the National Natural Science Foundation of China (No. 61922035, No. 11904118, No. 11874171). S.B.Z. was supported by the Department of Energy under Grant No. DE-SC0002623. J.B. was supported by Basic Science Research Program through the National Research Foundation of Korea (NRF-2018R1D1A1B07044564). The High-Performance Computing Center (HPCC) at Jilin University for calculation resources is acknowledged. We sincerely thank Prof. Sheng Meng in Institute of Physics (CAS) for supporting the TDDFT study.

AUTHOR CONTRIBUTIONS

X.P.W. and N.K.C. did the calculations. X.P.W., X.B.L., and S.B.Z. did the theoretical analyses. J.B. and N.K.C. offered the techniques of TDDFT simulations. R.N., C.E., and R.D. discussed the analyses of electronic bonding by the LOBSTER code. The paper is written by X.P.W., X.B.L., and S.B.Z. with the help of other authors. X.B.L. and H.B.S. proposed and initiated the project.

COMPETING INTERESTS

The authors declare no competing interests.

ADDITIONAL INFORMATION

Supplementary information is available for this paper at <https://doi.org/10.1038/s41524-020-0303-z>.

Correspondence and requests for materials should be addressed to X.-P.W., H.-B.S. or S.Z.

Reprints and permission information is available at <http://www.nature.com/reprints>

Publisher's note Springer Nature remains neutral with regard to jurisdictional claims in published maps and institutional affiliations.



Open Access This article is licensed under a Creative Commons Attribution 4.0 International License, which permits use, sharing, adaptation, distribution and reproduction in any medium or format, as long as you give appropriate credit to the original author(s) and the source, provide a link to the Creative Commons license, and indicate if changes were made. The images or other third party material in this article are included in the article's Creative Commons license, unless indicated otherwise in a credit line to the material. If material is not included in the article's Creative Commons license and your intended use is not permitted by statutory regulation or exceeds the permitted use, you will need to obtain permission directly from the copyright holder. To view a copy of this license, visit <http://creativecommons.org/licenses/by/4.0/>.

© The Author(s) 2020